Increasing impact of warm droughts on northern ecosystem productivity over recent decades

David Gampe[1,2*], Jakob Zscheischler[3,4,5], Markus Reichstein[6], Michael O'Sullivan[7], William K. Smith[8], Stephen Sitch[9] and Wolfgang Buermann[1,10]

[1]Institute of Geography, Augsburg University, 86159 Augsburg, Germany

[2]Department of Geography, Ludwig Maximilian University, 80333 Munich, Germany

[3]Climate and Environmental Physics, University of Bern, Sidlerstrasse 5, 3012, Bern, Switzerland

[4]Oeschger Centre for Climate Change Research, University of Bern, 3012, Bern, Switzerland

[5]Department of Computational Hydrosystems, Helmholtz Centre for Environmental Research – UFZ, Leipzig, Germany

[6]Max Planck Institute for Biogeochemistry, 07745 Jena, Germany

[7]College of Engineering, Mathematics and Physical Sciences, University of Exeter, Exeter EX4 4QF, UK

[8]School of Natural Resources and the Environment, University of Arizona, Tucson, AZ 85721, USA

[9]College of Life and Environmental Sciences, University of Exeter, Exeter EX4 4RJ, UK

[10]Institute of the Environment and Sustainability, University of California, Los Angeles, Los Angeles, CA 90095, USA

Corresponding author: David Gampe (david.gampe@googlemail.com)
Institute of Geography
Augsburg University
Alter Postweg 118
86159 Augsburg, Germany

Revised submission (Article) to

Nature Climate Change

Climate extremes such as droughts and heatwaves have a large impact on terrestrial carbon uptake by reducing gross primary production (GPP). While the evidence for increasing frequency and

intensity of climate extremes over the last decades is growing, potential systematic adverse shifts in GPP have not been assessed. Using an ensemble of observationally-constrained and process-based model data, here we show that particularly northern-midlatitude ecosystems experienced a +10.6 [+5.4|+14.6] % increase in negative GPP extremes in the period 2000 – 2016 compared to 1982 – 1998. We can attribute this increase to a greater impact of warm droughts, which affect GPP in and after the peak growing season. The related increase in negative GPP extremes is particularly strong over grasslands (+95.0 [+46.4|+172.2] % increase) and croplands (+84.0 [+70.7|+110.4] %). These results highlight the growing vulnerability of ecosystem productivity to warm droughts, implying increased adverse impacts of these extremes on terrestrial carbon sinks and a rising pressure on global food security.

Many climate extremes are projected to increase in frequency, intensity, and duration over the course of the 21st century [1,2,3]. For instance, recent studies project a significant increase in extreme heat events over most of the continents even by the year 2035 [4] and an increase in temperature-induced drought episodes over roughly half of global land for the period 2070 - 2100 [5]. These projected changes in climate extremes are consistent with observed trends. Particularly heatwaves and heavy precipitation events have already increased over the past decades [6,7,8,9]. In addition, increasing occurrences of synchronous hot and dry extremes [10], hotter droughts [11,12] and a temperature-induced intensification of dry seasons [13] were observed over the course of the last century. In this regard, the rising temperatures led to a substantial increase in the occurrence of compound warm season droughts over Europe during recent years [14].

Presently, the terrestrial biosphere acts as a prominent sink for anthropogenic CO_2 sequestering on average 25-30 % of the annual CO_2 emissions [15]. However, the potential for climate extremes to adversely impact ecosystems, and hence the terrestrial carbon sink, has been well documented [16]. A well-known example is the European drought and heat wave of 2003 that reduced plant productivity by 30 % thereby cancelling four years of carbon sink activity [17]. Further alterations of ecosystem functioning in forests through extreme droughts are caused by reduced growth rates with a legacy of up to four years [18] and potential stress fatigue during drought recovery [19]. The mounting evidence of more frequent and intense climate extremes and corresponding negative impacts on ecosystems in the recent past, raises the question whether such shifts in climate extremes have already led to systematic adverse shifts in plant productivity at regional and global scales.

Terrestrial gross primary production (GPP), the carbon flux entering the plants via photosynthesis, is the largest global carbon flux driving key ecosystem functions [20]. Yet, corresponding GPP estimates with global coverage are uncertain due to a lack of consistent large-scale observations and a limited understanding of the interacting drivers, processes and mechanisms that regulate GPP [21]. To account for this, the impacts of climate extremes on plant productivity were analyzed based on three global GPP ensemble data sets that are produced with different approaches in this study. These include two observationally-constrained GPP products, whereby one is based on upscaled eddy covariance flux tower measurements (FLUXCOM) [22, 23] and another is derived through a satellite-driven light use efficiency approach (LUE) [24]. The third GPP product represents an ensemble of twelve Dynamic Global Vegetation Models (DGVMs) as part of a recent model intercomparison project (TRENDYv6) [15] (see Methods for details).

Changes in negative GPP extremes over the past decades

To assess systematic shifts in GPP as a response to observed trends in climate extremes over the past decades, negative GPP extreme events were analyzed over the period 1982 – 2016. The detection of these events in each data set member followed a three-step procedure entailing (i), identifying local extremes at grid cell level, (ii) joining them through a flood-filling algorithm to form the negative GPP extreme events, (iii) retaining only the largest 1000 (in terms of cumulative negative GPP anomaly) of them for further analysis. This record of negative GPP extremes was then split in two study periods (1982-1998 and 2000-2016) to analyze changes in these extremes between the two epochs (see Methods).

Results showed that at regional scales, with a focus on the 26 regions designated in recent IPCC reports [25], consistent (i.e. all three data sets agree) increases in negative GPP extremes between the two study periods were found in eleven IPCC regions (Fig. 1). Hot spots of increasing negative GPP extremes, expressed as the difference in cumulative negative GPP anomaly between the two periods (ΔGPP [Pg C]), occurred in East Asia (EAS, -1.11 [-0.47|-1.51] Pg C; mean and [minimum|maximum] of the three data sets), Central North America (CNA, -0.46 [-0.20|-0.72] Pg C) and the Amazon region (AMZ, -0.85 [-0.27|-1.99] Pg C). Overall, the number of events increased in eight of these eleven regions (including CNA, EAS and AMZ; Fig. 1). A sensitivity analysis based on only the largest 100 negative GPP extreme events revealed similar patterns (see Supplementary Fig. S1-S3).

At larger spatial scales, the northern midlatitudes exhibited a consistent increase in negative GPP extremes between the two periods (-1.12 [-0.80|-1.40] Pg C; Fig. 2a, corresponding to a +10.6 [+5.4|+14.6] % increase; Fig. 2b). Over this broad domain, the number of extreme events did not show a consistent increase (Fig. 2c) implying a potential intensification of negative GPP extremes. Since previous studies on past climate extremes documented also pronounced seasonal changes [26, 27] that can alter GPP patterns [28], monthly and seasonal changes associated with negative GPP extremes over the northern midlatitudes were also assessed. Consistent significant (Mann-Whitney-U test, p-value < 0.05) increases in negative GPP extremes were found during the boreal summer month of August, with weaker evidence for such increases also in June and July (Fig. 2d-f). In addition, the seasonal characteristics revealed a consistent shift of the peak months for negative GPP extremes from June and July during the early period (1982 – 1998) to July and August during the second period (2000 – 2016; Fig. 2d-f).

Given the identified widespread regional increases in negative GPP extremes, their influence on the overall changes in climate-driven plant productivity [29] is of great interest. In this regard, an increase in negative GPP extremes can attenuate (exacerbate) a positive (negative) GPP trend. A corresponding analysis showed consistent climate-driven decreases in GPP in the period 2000 – 2016 (compared to 1982 – 1998) with strong exacerbation rates of 20 - 60 % across large portions of Western and Central North America as well as the Amazon and parts of East Asia (Supplementary Fig. S4). This suggests that over these regions increases in negative GPP extremes are responsible for a substantial portion of climate-driven GPP decreases. Increases in GPP between the two periods are attenuated (due to increases in negative GPP extremes) to some extent over Eastern Canada, Eastern Europe, portions of the Tropics and Southern Australia (Supplementary Fig. S4). In addition to a changing climate, plant productivity is also affected by changes in atmospheric CO_2 concentrations via CO_2 fertilization [30]. Because the three GPP datasets that are investigated here are not designed to capture this effect of rising CO_2 on GPP (instead they are devised to capture climate-driven GPP changes), additional TRENDY simulations that consider CO_2 fertilization were analyzed in a similar way (see Methods). Results based on this supplementary set of TRENDY simulations showed a spatially much more extensive pattern of positive GPP changes between the two study periods that are attenuated by the increase in negative GPP extremes (Supplementary Fig. S4). However, despite the generally beneficial effect of CO_2 on GPP, a strong exacerbation of overall negative GPP changes from increases in negative GPP extremes were still evident over Western and Central North America (Supplementary Fig. S4). These results suggest that at regional scales the influence of increased negative GPP extremes on cumulative GPP may be strong enough to effectively counteract positive CO_2 fertilization effects.

Attribution of changes in GPP extremes to climate drivers

Which climate drivers are then responsible for the identified increases in negative GPP extremes over recent decades? To answer this question, the negative GPP extreme events were attributed to climate drivers based on coinciding significant climate anomalies (see Methods). Here, concurrent anomalies in temperature and precipitation as well as meteorological drought (assessing the cumulative water deficit over longer durations) characterized through the Standardized Precipitation Index (SPI) [31] and the Standardized Precipitation Evapotranspiration Index (SPEI) [32] were considered. While the SPI captures only the effects of cumulative rainfall deficit or surpluses over a specified period, the SPEI also includes the effect of anomalous temperatures on drought severity through the inclusion of potential evapotranspiration (i.e. atmospheric demand). Droughts inferred from the SPEI are therefore also being referred to as "warm drought" in this study (see Methods).

At global scale and over the entire data record, the majority of the 1000 largest negative GPP events could be attributed to significant climate anomalies (68.7 % of the events, corresponding to 72.1 % of the total reduction in GPP; Supplementary Fig. S5). Thereby, the largest fraction (~50-60%) of the associated events and the corresponding GPP reduction could be attributed to drought conditions (estimated through SPEI and SPI) and a smaller fraction (~20%) to concurrent low precipitation (Supplementary Fig. S5). Other considered climate drivers, including concurrent high and low temperatures and concurrent high precipitation, did not show a significant association with negative GPP extremes and were thus not considered for further analysis (Supplementary Fig. S5; see Methods for details). However, a significant percentage of the identified droughts coincided with high temperatures over the second period (SPI: 26.7 [14.9|42.5] %; SPEI: 34.5 [19.9|52.4] %; Supplementary Fig. S5), implying an increased frequency of such compound events [10,14] that impacted GPP extremes over the recent decades.

In an ensuing spatially distributed analysis, the changes in negative GPP extremes (ΔGPP) associated with coinciding anomalies in any of the three significant climate drivers between the two periods were assessed. The patterns reveal that the marked increases in negative GPP extremes over Central North America and extensive parts of Eurasia and Australia are largely associated with drought (SPEI & SPI; Fig. 3a & b). In contrast, decreases in negative GPP extremes related to drought (SPEI & SPI) can be seen over Tropical Asia, large parts of Africa and parts of tropical South America (Fig. 3a & b). For concurrent low precipitation, the identified patterns were generally less pronounced with some evidence of increased impact on negative GPP extremes over Central North America, portions of Tropical South America and Eurasia and decreased impact over large portions of Africa (Fig 3c). In addition, when considering only the most likely (main) driver for a given event (based on the largest climate anomaly) increased impact of particularly warm droughts (SPEI) on GPP extremes were observed over large spatial extents of the northern midlatitudes, South Asia, South America as well as Australia (Supplementary Fig. S6). More contrasting patterns of increased impact were found for droughts assessed through the SPI and concurrent low precipitation (Supplementary Fig. S6).

The dominant role of droughts is also evident in the eleven IPCC regions that show consistent increased negative GPP extremes between the two periods (see Fig. 1). In ten of these regions (except for AMZ) an increasing impact of droughts (SPEI & SPI) was the main driver behind the increases in negative GPP extremes (Supplementary Fig. S7). This is also reflected in the relative contribution of each climate driver to the composition of negative GPP extremes attributable to climate anomalies. Here, specifically the contribution of warm droughts (in comparison to the other climate drivers) increased strongly in the second period in seven of these regions, most pronounced for MED (+24.1 %), CEU (+18.3 %) and EAS (+19.4 %; Fig. 4).

Taken together, warm droughts (SPEI) were identified as the key driver for the identified increases in negative GPP extremes (Fig. 4, Supplementary Fig. S6 and S7) over large areas of the northern midlatitudes, implying a widespread influence of warmer temperatures on exacerbating drought conditions that in turn cause increasing negative GPP extremes.

Given this substantial increased impact of warm droughts (SPEI) on GPP extremes over the northern midlatitudes, their seasonal characteristics were also examined. Results showed consistent increased impact of warm droughts across the boreal growing season months April through October in the 2000 – 2016 period compared to 1982 – 1998 (Supplementary Fig. S8). These increased impacts are statistically significant (Mann-Whitney-U test, p-value < 0.05) for July in all three data sets and from April to August for TRENDY and LUE. The boreal summer months June and July (peak months of drought impact) showed the largest increase in negative GPP response to warm drought accompanied by an intensification of drought influence in August (highest relative increase between the two periods; Supplementary Fig. S8) implying an extension of the drought season. The identified tendency of increased drought influence in the early part of the growing season could be a response to earlier and warmer springs [34, 35]. The increasing drought vulnerability during the later portion of the growing season could be due to rising water limitations as temperature constraints on plant growth diminish (due to general warming) and higher soil water is needed to support plant growth [36]. In addition, earlier springs and higher early season plant productivity can induce lagged effects that cause soil moisture depletion and increased drought impacts on GPP in the late summer months [37, 38].

Changes in GPP extremes for specific vegetation types

In general, hydrometeorological extremes such as droughts can adversely impact plants in two main interconnected ways. First, the deficit of available water directly impacts plant growth and can potentially cause hydraulic failure, resulting in often irreversible desiccation of the plant [39]. Second, plants may react to soil water shortages or increased atmospheric demand [40] with stomatal closure to prevent this desiccation, leading to a decline in photosynthetic carbon uptake, a process known as carbon starvation [39]. In this regard, the vegetation type can modulate the impact of climate anomalies on GPP [41]. A corresponding analysis stratified by vegetation types revealed the most substantial consistent increases in negative GPP extremes between the two periods (ΔGPP) over northern temperate grasslands (-0.64 [-0.21|-1.15] Pg C; +34.0 [+17.8|+45.1] % increase) and croplands (-0.58 [-0.18|-0.99] Pg C; +25.1 [+12.9|+36.5] %) indicating a higher vulnerability of these land covers (Fig. 5a-b). Warm droughts (SPEI) were identified as the main driver of increased negative GPP extremes and of their occurrences across vegetation types and data sets (Fig. 5c). These changes in negative GPP extremes attributed to SPEI were significant (two-sided t-test, p-value < 0.05) for grasslands (-0.63 [-0.27|-1.04] Pg C; +95.0 [+46.4|+172.2] % increased impact of warm droughts) and croplands (-0.73 [- 0.28|-1.30] Pg C; +84.0 [+70.7|+110.4] %) in all three data sets (Fig. 5c). Overall, results using SPI to identify droughts resulted in similar but less consistent patterns (Fig. 5d). No substantial impacts of concurrent low precipitation on the increases in negative GPP extremes could be identified (Fig. 5e). The identified higher vulnerability of grasslands and croplands to hydrometeorological extremes (specifically warm droughts) may be due to a lower coping capacity in respect to water scarcity compared to woody vegetation due to shallower roots and thus more limited access to deeper soil water [42]. Consequently, these vegetation types typically show a faster and more direct response to droughts in general and a stronger GPP reduction with temperatures exceeding optimal conditions [43]. In addition, particularly intensive cropland areas were found to be vulnerable to climate variations [44] and hydrometeorological extremes as the focus on yield and growth maximization, through high stomatal conductance, decreases their acclimatization ability to adverse climate conditions [45].

The identified adverse impact of droughts on GPP over croplands can potentially be mitigated through management practices, such as irrigation [46]. However, except for the LUE data set (which indirectly captures management activities through the assimilation of satellite vegetation data; see Methods), the considered GPP data sets do not account for such land management activities. Therefore, an additional set of TRENDY DGVMs with enabled land management and land use changes was analyzed (see Methods). Results based on this supplementary analysis showed lower increases in negative GPP extremes in the DGVMs with enabled land management compared to their climate-driven model counterparts (Fig. 5f; negative GPP extremes are reduced by 0.34 [0.1|0.82 Pg C or 53.1 [16.9|96.0] % in this comparison). The results further suggest that land management options such as irrigation can mitigate the impact of warm droughts (SPEI) on GPP extremes to some extent (Fig. 5f). In contrast, results based on the observationally-constrained LUE GPP data set (that captures management activities indirectly) suggest a relatively high adverse response of GPP to drought over croplands (Fig. 5c, d). Restricting the analysis to permanently irrigated areas only showed a near cancellation of warm drought impacts on GPP when irrigation is enabled (Fig. 5f). However, these regions are spatially limited to large river basins (representing 17% of the global cropland area [47]) and the DGVMs assume limitless water availability over these regions (e.g. via implicit irrigation through assumptions of zero plant water stress [48]). Taken together, these results indicate a higher vulnerability of grasslands and croplands to drought conditions and that the ability to buffer related impacts through present-day land management practices (e.g., irrigation) over croplands is limited.

In summary, the presented results showed that large portions of the continents experienced increased adverse impacts on plant productivity that can be attributed to climate extremes over the last decades. In this context, the most robust imprints were found over the northern midlatitudes, where particularly the hot spot regions Western and Central North America (WNA, CNA) and Eastern Asia (EAS) are affected by severe increases in negative GPP extremes. In agreement with the recent increase of temperature-driven droughts [14] we identified warm droughts (SPEI) as the main driver of consistent and widespread increases in negative GPP extremes over the periods 2000 – 2016 compared to 1982 – 1998, particularly over the northern midlatitudes. Previous studies projected severe increases in negative GPP extremes by the end of the 21st century [49] that are attributed to drought impacts [50] over North and South America, parts of Europe and East Asia. Our results suggest that these projected increased adverse impacts on GPP related to drought extremes may already be ongoing. Furthermore, negative GPP extremes play a crucial role in the modulation of GPP trends by exacerbating climate-driven negative GPP trends as well as attenuating the positive impact of CO_2 fertilization, implying a rising threat to the stability of the land carbon sink [16]. This is particularly worrisome over the identified hot spot regions (WNA, CNA & and partly EAS) where the increased GPP extremes overrides a potential positive effect of CO_2 fertilization.

The most severe increases in negative GPP extremes were identified over grasslands and croplands of the northern midlatitudes. Particularly the strong and consistent increases over croplands underscore the need for vast and swift deployment of adaptation measures to increase drought resilience of agricultural areas. Such adaptation measures might include the reduction of monocultural cropping [51], optimizing the use of existing resources [52] as well as societal coping capacities [53]. Additionally, biotechnological enhanced drought-resistance crop types [53, 54] might be unavoidable to increase drought resilience of agricultural areas under climate change. The presented results thus urge for societal actions to guarantee stable agricultural productivity easing potential pressures on global food security.

Methods

GPP data sets

Three state-of-the-science global GPP data sets spanning a 35-year period (1982 **–** 2016) were applied in this study. While these data sets were produced with different methodologies, they share a common meteorological input data set (CRUNCEPv8; https://vesg.ipsl.upmc.fr/thredds/catalog/work/p529viov/cruncep/V8_1901_2016/catalog.htm).

The first were GPP data produced through upscaling of local eddy covariance carbon flux tower measurements (224 sites globally distributed), that measure net carbon exchange between land and the atmosphere, to global fields using machine-learning methods with gridded climate and satellite data as inputs (FLUXCOM RS+METEO) [22, 23]. The upscaling process was performed by three machine learning methods: Artificial Neural Networks, Random Forests, and Multivariate Adaptive Regression [22, 23]. The component GPP fluxes were then derived through the estimation of the temperature sensitivity of ecosystem respiration (TER) from nighttime flux data and the resulting daytime extrapolation is used to determine GPP [55]. In the FLUXCOM RS+METEO GPP product the interannual variability and trend patterns are derived from time-varying meteorological input variables exclusively, while only the seasonal cycle of plant growth is constrained by satellite vegetation data [22]. The FLUXCOM RS+METEO GPP product hence does not include associated effects of CO_2 fertilization [22] and solely captures the response of GPP to instantaneous climate variability to a large degree while not including vegetation and lagged soil moisture effects. The FLUXCOM ensemble analyzed here consisted of three different GPP estimates (members) based on the different upscaling algorithms and their spread was used as a measure of uncertainty.

Second, a satellite-driven Light Use Efficiency (LUE) model based on the MODIS GPP algorithm driven by bimonthly time varying satellite GIMMS FPAR3g (LUE-FPAR3g) [24] was used. Complementary meteorological driver data (in addition to CRUNCEPv8) required as input were derived from NCEP-DOE Reanalysis II (http://www.esrl.noaa.gov). Additional information on the GIMMS3g GPP data set can be found in the referenced studies [24, 29]. Further, the Fraction of absorbed Photosynthetic Active Radiation (FPAR), based on the Normalized Difference Vegetation Index version 3g data set (NDVI3g) from NOAA-AVHRR satellites using a neural network algorithm is considered as model input [56]. Importantly for this study, the MODIS GPP algorithm assumes a temporally invariant LUE, and therefore does not capture the direct effect of atmospheric CO_2 increase on GPP (via an increase in LUE) [57]. Consequently, changes in GPP based on satellite-driven LUE data are largely driven by climate variability and changes in FPAR. In contrast to FLUXCOM, vegetation memory effects are thus at least partly included (as bimonthly time varying FPAR is used) and therefore may represent an additional source of uncertainty. The LUE GPP ensemble analyzed here consisted of two GPP members derived through varied model parameters within known constraints [24] and the spread of these two members was used as a measure of uncertainty.

Third, GPP data from twelve DGVMs that were part of the TRENDYv6 multi-model inter-comparison and followed a common protocol [58] were used. Models included in the TRENDYv6 ensemble analyzed in this study are CABLE [59], CLASS-CTEM [60], CLM4.5-BGC [61], DLEM [62], ISAM [63], LPJ-GUESS [64], JSBACH [65], JULES [66], ORCHIDEE [67], ORCHIDEE-MICT [68], VEGAS [69], and VISIT [70]. Here, the *CO_2 only* (S1 experiments) and *Climate and CO_2* (S2 experiments) simulations for the entire set of TRENDYv6 simulations were used to derive the climate-driven GPP portion in the TRENDYv6 model runs (consistent with the study aim). The *CO_2 only* simulations were driven with time varying observed atmospheric CO_2 concentrations using static meteorological data from the early 20th century (1901-1920; CRUNCEPv8), thus do not capturing changes in climate over the historical period. To derive the climate only response for each model, the exponential trend in GPP, for each month, over the analyzed 35 years (1982 – 2016) for each grid cell in these *CO_2 only* simulations was subtracted from the corresponding *Climate and CO_2* simulation. This procedure thus preserved the variability arising from climate variations but removed the influence of a potential trend in CO_2 concentrations over the study period. The TRENDY GPP ensemble analyzed in this study consisted of twelve GPP estimates (members, derived from the twelve TRENDYv6 DGVMs in the presented way); the spread of these members was used as a measure of uncertainty.

It is important to note that the TRENDY simulations (*CO_2 only* as well as *climate and CO_2*) use a fixed preindustrial landcover distribution and the climate-driven GPP product derived from those simulations therefore did not include potential effects introduced by any recent land-use and landcover changes (LULCC). This is consistent with FLUXCOM but contrasts to some extent with the LUE GPP product that does capture LULCC effects as well as land management practices (e.g. irrigation) indirectly via the satellite-derived FPAR. Further, all three global GPP data products included were driven by surface air temperature, while only the TRENDY and FLUXCOM GPP simulations also used precipitation as a meteorological model input. In the LUE GPP estimates, a vapor-pressure deficit (VPD) scalar was used to represent moisture limitations [24].

To estimate the potential of land management activities to mitigate drought impact over croplands via irrigation, a supplementary set of TRENDY simulations driven with temporally varying *climate & CO_2 & land use / land management* (S3 experiments) [58] was used. Here, only the three DGVMs that represent land management activities (DLEM [62], ISAM [63], LPJ-GUESS [64]) were analyzed whereby the same preprocessing procedure was applied to remove to remove the GPP trend arising from CO_2 fertilization (derived from the *CO_2 only* TRENDY simulations). Corresponding results of this supplementary analysis shown in Fig. 5f thus refer to these three DGVMs only.

Analysis framework for detection of GPP extremes and attribution of climate drivers

Pre-processing of the data

All data sets analyzed in this study were harmonized to a common 0.5° grid. As the focus was on detecting negative GPP extremes (i.e., the cumulative GPP anomaly of a corresponding negative GPP extreme event), the linear trend was removed from all GPP data sets individually to avoid misleading results due to a regional positive (or negative) climate-induced trend that shifts the overall mean. In contrast, the meteorological data sets applied for the attribution of negative GPP extremes were not detrended to allow for a detection of potential impacts of changes in climate extremes. Additionally, as Earth observation data are characterized by distinguishable seasonality [71, 72], the seasonal cycle was subtracted from all data sets for each grid cell. Precipitation and temperature have additionally been normalized by the standard deviation, to allow for spatial comparability, when applied to address concurrent effects of temperature and precipitation. GPP was not normalized to assess the cumulative negative GPP extremes in the unit of Pg C.

Detection of negative GPP extremes and characterization of events

In general, "extremes" are defined as the occurrence of anomalies of a given variable (e.g. GPP) above or below a given threshold at the ends of the distribution function of observed values [73]. The assessment of negative GPP extreme events followed a three-step procedure in this study where all steps were carried out for each member of each data set individually. First, local extremes were detected using a 10^{th} percentile threshold at grid cell level and classified according to the occurrence of anomalies below/above that threshold. Thereby, negative GPP extremes have been identified for each time step and for each grid cell. In the second step, a flood-filling algorithm was applied [74] to detect spatio-temporally connected grid cells classified as negative GPP extremes which are then joined to form the same event. The resulting 3-dimensional negative GPP extreme events, now extended in space and time, were assigned their respective cumulative GPP anomaly. Third, only the globally largest 1000 events based on their cumulative GPP anomaly were retained for all subsequent analyses presented in the manuscript, as generally few extreme events dominate the aggregated impact [72]. The detection of local extremes in the first step of our approach limits the overestimation of high-variance regions, compared to the application of global thresholds [75] while the subsequent steps still ensure that events of global relevance are selected. Further, the data were split into two periods of equal length (1982 – 1998 and 2000 – 2016) and the cumulative negative GPP extremes were calculated for each period separately. To then assess the changes in the corresponding cumulative GPP anomalies (ΔGPP) between the two study periods, they were subtracted from one another (2000 – 2016 minus 1982 – 1998). The year 1999 was excluded on purpose to ensure periods of equal length and avoid potential temporal overlaps of events that might then occur and be counted in both periods.

Unless stated otherwise, the most robust estimates, defined as the median across all members of a given data set ensemble, were presented in the manuscript. The presented results throughout the manuscript were derived as the mean [minimum|maximum] of those medians, unless stated otherwise. The same procedure was applied to derive the figures presented in the manuscript and the supplement. To complement this, the analysis was also conducted using only the largest 100 events (Supplementary Fig. 1-3) to test the robustness of the results as the selection of a given number of events is somewhat arbitrary.

Attribution of drivers

Next, the identified GPP extreme events were attributed to climate drivers. In consistency with the meteorological forcing of the three GPP data sets analyzed in this study, the CRUNCEPv8 data set (https://vesg.ipsl.upmc.fr/thredds/catalog/work/p529viov/cruncep/V8_1901_2016/catalog.htm) was used. Precipitation, air temperature, and meteorological drought were considered as potential climate drivers of negative GPP extreme events. Thereby, an event was attributed to *concurrent low* and *high temperature* (*precipitation*, respectively) if a coinciding significant (p-value <0.1 and >0.9, respectively) temperature (precipitation) anomaly was detected over the spatial domain of the GPP extreme event [72]. While a concurrent water deficit can be at least partly considered as drought, we referred to low precipitation anomalies as *concurrent low precipitation* as the duration of the water deficit in case of this indicator was solely based on the time step of the meteorological data set (in our case one month). We thus followed previous studies [33,74] and considered it appropriate to distinguish between the short term, immediate and concurrent water deficit (that is "concurrent low precipitation") and more severe and sustained drought conditions that were derived from two indicators to detect multi-month meteorological drought conditions.

First, to capture anomalies in long-term water budgets only, the Standardized Precipitation Index (SPI) [31] was applied. Negative GPP extreme events were attributed to the *SPI* through detection of significant (p-value 0.1 and 0.9, respectively) anomalies in the 3-, 6- or 12-month SPI values. The considered time scales in the calculation of the SPI with up to 12 months were found to allow for a robust attribution of GPP extremes. The inclusion of longer time scales (24-month SPI) did not yield additional attributions of GPP extreme events that were not already captured by the shorter calculation time scales applied. In contrast, the full recovery time of the ecosystems potentially spans a much larger time scale up to multiple years [19] however, this ecological response was outside the study scope and not detected as part of the GPP extreme events in this study.

Second, the Standardized Precipitation Evapotranspiration Index (SPEI), which estimates a climatic water balance through the difference of precipitation and potential evapotranspiration [32], derived through the Thornwaite equation [76], was used. Like SPI, GPP extreme events were attributed to *SPEI* through significant (p-value 0.1) anomalous 3-, 6- or 12-month SPEI values. The main difference between these two drought indicators is the inclusion (absence) of temperature information in the calculation of SPEI (SPI), respectively. Major differences in the resulting anomalies of those two indicators can thus be interpreted as a temperature imprint on the corresponding drought event through its impact on potential evapotranspiration. Thereby, coinciding higher, but not necessarily extreme, temperatures (leading to increased potential evapotranspiration) result in stronger negative anomalies in the SPEI. Therefore, drought characterized through SPEI is also referred to as "warm drought" throughout the study.

Potentially, multiple climate drivers show anomalous behavior during a negative GPP extreme event and thus can be counted toward the attribution of that event. The findings on climate attribution and corresponding impacts on negative GPP extremes therefore included multiple countings per event (e.g., if coinciding anomalies in *concurrent low precipitation* and *SPEI* were detected, the corresponding GPP event was assigned to both). Additionally, also the climate driver showing the strongest anomaly for a given GPP extreme event was singled out and referred to as the most likely (or main) driver of a particular negative GPP extreme event.

Given the defined threshold of 10 and 90 % (assessment through the p-values) for the detection of significant climate anomalies, an attribution of 10 % of the GPP extremes to a given climate driver would be expected if no association were present. Therefore, drivers that did not show an association rate higher than 10 % were considered insignificant in the attribution of GPP extreme events. In the analysis, a consistent significant contribution of *concurrent high* and *low temperature* extremes as potential drivers of negative GPP extremes was absent (see also Supplementary Fig. S5). Thus both, *concurrent high* and *low* temperature were excluded from subsequent analysis. Similarly, positive SPI and *concurrent high precipitation* were excluded as potential drivers.

Land Cover and land management analysis

The Moderate Resolution Imaging Spectroradiometer (MODIS) Land Cover Climate Modeling Grid (CMG) (MCD12C1) Version 6 data set [77] was applied to address the impacts of climate extremes on negative GPP extremes over different vegetation types in this study. This data product provides a time series of annual global land cover maps for the period 2001-2018. Thereby, the year 2001 assessed through the International Geosphere-Biosphere Programme (IGBP) classification scheme was selected as baseline for the analyses carried out in this study. This map was aggregated to a 0.5-degree grid (using a maximum area fraction approach), to match the resolution of the applied GPP and climate data sets. In addition, the aggregated MCD12C1 maps of the years 2001 – 2016 were applied to detect areas affected by land cover changes over the study period. Thereby, only a few grid cells were detected at the coarse target resolution (0.5 degrees) and were consequently masked in the final land cover map applied in this study. These masked areas have been excluded from the land cover analyses and all presented results in the manuscript. Further, only vegetated land cover classes covering at least 5% of the area of the northern midlatitudes (23.5 -66.0 °N) were considered in this analysis to avoid biases in presented percentage changes introduced by a single extreme events. The resulting cumulative changes in GPP extremes were calculated as the difference of negative GPP extremes over each considered land cover class between the two periods (2000 – 2016 to 1982 – 1998) to assess changes in vulnerability. Differences presented as delta-plots were based on absolute changes in the number of events (for each climate driver and over each land cover class) and negative GPP extremes (cumulative negative GPP anomalies [Pg C]) between the two periods. Significance testing (two-sided t-test, p-value < 0.05) was performed to assess differences in the mean for monthly GPP anomalies between the two periods (for each climate driver and over each land cover class) for the median of each ensemble.

To address the effectiveness of land management actions, such as irrigation, to mitigate drought impact, the corresponding simulations (*climate & CO_2 & land use / land management*; S3 experiments) [58] of the three TRENDY models that that explicitly consider management (DLEM [62], ISAM [63], LPJ-GUESS [64]) were used to derive negative GPP extreme events following the previously described procedure including removing the CO_2 trend as well as seasonal effects. Only stable cropland areas in the models were considered in this specific analysis to avoid uncertainties introduced by land cover change occurring in the simulations over the study period. A stable cropland area was thereby detected if the cropland fraction within the corresponding grid cell exceeded 50% over the entire period (1982 – 2016) in the respective TRENDY simulation. The same approach was conducted on the corresponding simulations of the three DGVMs with *climate-only* forcing. In this way, these two data set ensembles only differed in the inclusion of management options. Hence both ensembles allowed for a meaningful comparison and differences between those two could be interpreted as an estimation of the effectiveness of such management options to mitigate drought impact on GPP extremes. However, irrigation in DGVMs is often implicit [78], by assuming no plant water stress / zero root zone water deficit, and this may be considered optimal irrigation management, i.e. represent the maximum potential mitigation ability through elevating soil water deficit.

Acknowledgements

J.Z. has been supported by the Swiss National Science Foundation (grant no. 179876) and the Helmholtz Initiative and Networking Fund (Young Investigator Group COMPOUNDX, Grant Agreement VH-NG-1537). S.S. has been supported by the Newton Fund through the Met Office Climate Science for Service Partnership Brazil (CSSP Brazil). W.K.S. acknowledges funding from NASA Terrestrial Ecosystems Grant 80NSSC19M0103.

Author Contributions

D.G. and W.B. developed the conceptual framework of this research project. D.G. carried out the data analysis with M.O'S. and W.K.S. providing the pre-processed GPP and climate data sets. D.G. drafted the initial version of the manuscript, and all authors contributed to writing the final paper and the interpretation of the results.

Competing Interests

The authors declare no competing interests.

Data Availability

The TRENDY v6 data sets applied in this study have been pre-processed by M.O'S. and are available upon reasonable request. The original TRENDY v6 data sets can be requested from Stephen Sitch (s.a.sitch@exeter.ac.uk) and Pierre Friedlingstein (p.friedlingstein@exeter.ac.uk). The FLUXCOM data set is publicly available through the FLUXCOM data portal (https://www.bgc-jena.mpg.de/geodb/projects/FileDetails.php). The LUE data sets are provided by W.K.S. and publicly available at https://wkolby.org/data-code/. The CRUNCEP reanalysis data is available through the Climatic Research Unit data portal (https://crudata.uea.ac.uk/cru/data/ncep/#dataset_access).

Code Availability

All relevant codes are available from D.G. upon request.

References

[1] Sillmann, J., Kharin, V. V., Zwiers, F. W., Zhang, X. & Bronaugh, D. Climate extremes indices in the CMIP5 multimodel ensemble: Part 2. Future climate projections. *J. Geophys. Res.: Atm.* **118**, 2473-2493 (2013).

[2] Lehmann, J., Coumou, D. & Frieler, K. Increased record-breaking precipitation events under global warming. *Clim. Change* **132**, 501-515 (2015).

[3] Yin, J. et al. Large increase in global storm runoff extremes driven by climate and anthropogenic changes. *Nat. Commun.* **9**, 1-10 (2018).

[4] Fischer, E. M. Beyerle, U. & Knutti, R. Robust spatially aggregated projections of climate extremes. *Nat. Clim. Change* **3**, 1033-1038 (2013).

[5] Spinoni, J. et al. Future global meteorological drought hotspots: a study based on CORDEX data. *J. Clim.* **33**, 3635-3659 (2020).

[6] Coumou, D. & Rahmstorf, S. A decade of weather extremes. *Nat. Clim. Change* **2**, 491-496 (2012).

[7] Alexander, L. V. Global observed long-term changes in temperature and precipitation extremes: A review of progress and limitations in IPCC assessments and beyond. *Weather Clim. Extremes* **11**, 4-16 (2016).

[8] Seneviratne, S. I., Donat, M. G., Mueller, B. & Alexander, L. V. No pause in the increase of hot temperature extremes. *Nat. Clim. Change* **4**, 161 - 163 (2014).

[9] Barriopedro, D., Sousa, P. M., Trigo, R. M., García-Herrera, R. & Ramos, A. M. The exceptional Iberian heatwave of summer 2018. *Bull. Amer. Meteor. Soc.* **101**, 29-34 (2020).

[10] Alizadeh, M. R., et al. A century of observations reveals increasing likelihood of continental-scale compound dry-hot extremes. *Sci. Adv*. **6**, eaaz4571 (2020).

[11] Allen, C. D., Breshears, D. D. & McDowell, N. G. On underestimation of global vulnerability to tree mortality and forest die-off from hotter drought in the Anthropocene. *Ecosph.* **6**, 1-55 (2015).

[12] Chiang, F., Mazdiyasni, O. & AghaKouchak, A. Amplified warming of droughts in southern United States in observations and model simulations. *Sci adv.* **4**, eaat2380 (2018).

[13] Padrón, R. S., et al. Observed changes in dry-season water availability attributed to human-induced climate change. *Nat. Geosci.* **13**, S. 477-481 (2020).

[14] Markonis, Y., et al. The rise of compound warm-season droughts in Europe. *Sci. Adv.* **7**, eabb9668 (2021).

[15] Le Quéré, C., et al. Global carbon budget 2017. *Earth Syst. Sci. Data.* **10**, 405-448 (2017).

[16] Reichstein, M., et al. Climate extremes and the carbon cycle. *Nature* **500**, 287-295 (2013).

[17] Ciais, P., et al. Europe-wide reduction in primary productivity caused by the heat and drought in 2003. *Nature* **437**, 529-533 (2005).

[18] Anderegg, W. R., et al. Pervasive drought legacies in forest ecosystems and their implications for carbon cycle models. *Science* **349**, 528-532 (2015).

[19] Schwalm, C. R., et al. Global patterns of drought recovery. *Nature* **548**, 202-205 (2017).

[20] Jia, G. E., et al. Land–climate interactions. Climate Change and Land: an IPCC special report on climate change, desertification, land degradation, sustainable land management, food security, and greenhouse gas fluxes in terrestrial ecosystems, Shukla, P.R., et al. (eds.) 131-247 (2019).

[21] Ryu, Y., Berry, J. A. & Baldocchi, D. D. What is global photosynthesis? History, uncertainties and opportunities. *Remote Sens. Environ.* **223**, 95-114 (2019).

[22] Tramontana, G., et al. Predicting carbon dioxide and energy fluxes across global FLUXNET sites with regression algorithms. *Biogeosc.* **13**, 4291–4313 (2016).

[23] Jung, M., et al. The FLUXCOM ensemble of global land-atmosphere energy fluxes. *Sci. Dat.* **6**, 1-14 (2019).

[24] Smith, W. K., et al. Large divergence of satellite and Earth system model estimates of global terrestrial CO 2 fertilization. *Nat. Clim. Change* **6**, 306-310 (2016).

[25] Field, C. B., Barros, V., Stocker, T. F., Dahe, T. F. Managing the risks of extreme events and disasters to advance climate change adaptation: special report of the intergovernmental panel on climate change. (Cambridge Univ. Press, Cambridge, 2012).

[26] Alexander, L. V., et al. Global observed changes in daily climate extremes of temperature and precipitation. *J. Geophys. Res.: Atm.* **111** (2006).

[27] Orlowsky, B. & Seneviratne, S. I. Global changes in extreme events: regional and seasonal dimension. *Clim. Change* **110**, 669-696 (2012).

[28] Piao, S., Friedlingstein, P., Ciais, P., Viovy, N., & Demarty, J. Growing season extension and its impact on terrestrial carbon cycle in the Northern Hemisphere over the past 2 decades. *Glob. Biogeoch. Cyc.* **21** (2007).

[29] O'Sullivan, M., et al. Climate-driven variability and trends in plant productivity over recent decades based on three global products, *Glob. Biogeochem. Cyc.*, **34**, (2020).

[30] Walker, Anthony P., et al. Integrating the evidence for a terrestrial carbon sink caused by increasing atmospheric CO_2. *New Phytol.* (2020).

[31] McKee, T. B., Doesken, N. J. & Kleist, J. The relationship of drought frequency and duration to time scales. *Proc. 8th Conf. Appl. Clim.* **17**, 179-183 (1993).

[32] Vicente-Serrano, S. M., Beguería, S. & López-Moreno, J. I. A multiscalar drought index sensitive to global warming: the standardized precipitation evapotranspiration index. *J. Clim.* **23**, 1696–1718 (2010).

[33] Zscheischler, J., et al. Extreme events in gross primary production: a characterization across continents. *Biogeosc.* **11**, 2909-2924 (2014).

[34] Menzel, A., et al. European phenological response to climate change matches the warming pattern. *Glob. Change Biol.* **12**, 1969-1976 (2006).

[35] Choi, W. & Kim, K. Y. Physical mechanism of spring and early summer drought over North America associated with the boreal warming. *Sci. Rep.* **8**, 1-8 (2018).

[36] Zhang, Y., Parazoo, N. C., Williams, A. P., Zhou, S., & Gentine, P. Large and projected strengthening moisture limitation on end-of-season photosynthesis. *Proc. Natl. Acad. Sci.* **117**, 9216-9222 (2020).

[37] Buermann, W., et al. Widespread seasonal compensation effects of spring warming on northern plant productivity. *Nature* **562**, 110-114 (2018).

[38] Bastos, A., et al. Direct and seasonal legacy effects of the 2018 heat wave and drought on European ecosystem productivity. *Sci. Adv.* **6** (2020).

[39] McDowell, N., et al. Mechanisms of plant survival and mortality during drought: why do some plants survive while others succumb to drought? *New Phytol.,* **178**, 719-739 (2008).

[40] Yuan, W., et al. Increased atmospheric vapor pressure deficit reduces global vegetation growth. *Sci. Adv.* **5,** eaax1396 (2019).

[41] Flach, M., et al. Vegetation modulates the impact of climate extremes on gross primary production. *Biogeosci*. **18**, 39-53 (2021).

[42] He, W., et al. Large-scale droughts responsible for dramatic reductions of terrestrial net carbon uptake over North America in 2011 and 2012. *J. Geophys.Res.: Biogeosci.* **123**, 2053-2071 (2018).

[43] Sippel, S., et al. Drought, heat, and the carbon cycle: a review. Curr. Clim. Change Rep. 4, 266-286 (2018).

[44] Ray, D. K., Gerber, J. S., MacDonald, G. K., & West, P. C. Climate variation explains a third of global crop yield variability. *Nat. commun.* **6**, 1-9 (2015).

[45] Schwalm, C. R., et al. Assimilation exceeds respiration sensitivity to drought: A FLUXNET synthesis. *Glob. Change Biol.* **16**, 657-670 (2010).

[46] van der Velde, M., Wriedt, G., & Bouraoui, F. Estimating irrigation use and effects on maize yield during the 2003 heatwave in France. *Agricult., Ecosys. & Env.* **135**, 90-97 (2010).

[47] Bondeau, A., et al. Modelling the role of agriculture for the 20th century global terrestrial carbon balance. *Glob. Change Biol*. **13,** 679-706 (2007).

[48] Hurtt, G. C., et al. Harmonization of global land use change and management for the period 850–2100 (LUH2) for CMIP6. *Geosci. Mod. Dev.* **13,** 5425- 5464 (2020).

[49] Zscheischler, J., et al. Carbon cycle extremes during the 21st century in CMIP5 models: Future evolution and attribution to climatic drivers. *Geophys. Res. Let.* **41**, 8853-8861 (2014).

[50] Xu, C., et al. Increasing impacts of extreme droughts on vegetation productivity under climate change. *Nat. Clim. Change* **9**, 948-953 (2019).

[51] Lesk, C., Rowhani, P. & Ramankutty, N. Influence of extreme weather disasters on global crop production. *Nature* **529**, 84-87 (2016).

[52] Mueller, N., Gerber, J., Johnston, M., Ray, D., Ramankutty, N. & Foley, J. Closing yield gaps through nutrient and water management. *Nature* **490**, 254–257 (2012).

[53] Meza, I., et al. Global-scale drought risk assessment for agricultural systems. *Nat. Haz.Earth Syst. Sci.* **20** (2020).

[53] Martignago, D., Rico-Medina, A., Blasco-Escaméz, D., Fontanet-Manzaneque, J. B. & Caño-Delgado, A. I. Drought resistance by engineering plant tissue-specific responses. *Front. Plant Sci.* **10**, 1676 (2019).

[54] Gupta, A., Rico-Medina, A., & Caño-Delgado, A. I. The physiology of plant responses to drought. *Science* **368**, 266-269 (2020).

References for Methods section

[55] Reichstein, M., et al. On the separation of net ecosystem exchange into assimilation and ecosystem respiration: review and improved algorithm. *Glob. Change Biol.* **11**, (2005).

[56] Zhu, Z., et al. Global data sets of vegetation leaf area index (LAI) 3g and fraction of photosynthetically active radiation (FPAR) 3g derived from global inventory modeling and mapping studies (GIMMS) normalized difference vegetation index (NDVI3g) for the period 1981 to 2011. *Remote Sens.* **2**, 927-948 (2013).

[57] Smith, W. K., Fox, A. M., MacBean, N., Moore, D. J. & Parazoo, N. C. Constraining estimates of terrestrial carbon uptake: new opportunities using long-term satellite observations and data assimilation. *New Phytol.* **225**, 105-112 (2019).

[58] Sitch, S., et al. Recent trends and drivers of regional sources and sinks of carbon dioxide. *Biogeosci.* **12**, 653-679 (2015).

[59] Haverd, V., et al. A new version of the CABLE land surface model (Subversion revision r4601) incorporating land use and land cover change, woody vegetation demography, and a novel optimisation-based approach to plant coordination of photosynthesis. *Geosc. Mod. Dev.* **11**, 2995-3026 (2018).

[60] Melton, J. R. & Arora, V. K. Competition between plant functional types in the Canadian Terrestrial Ecosystem Model (CTEM) v. 2.0. *Geosc. Mod. Dev.* **9**, 323–361 (2016).

[61] Oleson, K. W., et al. Technical Description of version 4.5 of the Community Land Model (CLM). *NCAR Technical Note: NCAR/TN-503+ STR* (2013).

[62] Tian, H., et al. North American terrestrial CO2 uptake largely offset by CH4 and N2O emissions: toward a full accounting of the greenhouse gas budget*.* *Clim. Change* **3–4**, 413–426 (2015).

[63] Jain, A. K., Meiyappan, P., Song, P., House, J. I. CO 2 emissions from land-use change affected more by nitrogen cycle, than by the choice of land-cover data. *Glob. Change Biol.* **19**, 2893–2906 (2013).

[64] Smith, B., et al. Implications of incorporating N cycling and N limitations on primary production in an individual-based dynamic vegetation model. *Biogeosc.* **11**, 2027–2054 (2014).

[65] Reick, C. H., Raddatz, T., Brovkin, V. & Gayler, V. Representation of natural and anthropogenic land cover change in MPI-ESM. *J. Adv. Mod. Earth Syst.* **5**, 459–482 (2013).

[66] Clark, D. B., et al. The Joint UK Land Environment Simulator (JULES), model description—Part 2: carbon fluxes and vegetation dynamics. *Geosc. Mod. Dev.* **4**, 701-722 (2011).

[67] Krinner, G., et al. A dynamic global vegetation model for studies of the coupled atmosphere-biosphere system, *Glob. Biogeoch. Cyc.* **19**, (2005).

[68] Guimberteau, M., et al. ORCHIDEE-MICT (v8.4.1), a land surface model for the high latitudes: model description and validation. *Geosc. Mod. Dev.* **11**, 121-163 (2018).

[69] Zeng, N., Mariotti, A. & Wetzel, P. Terrestrial mechanisms of interannual CO2 variability. *Glob. Biogeoch. Cyc.* **9** (2005).

[70] Kato, E., Kinoshita, T., Ito, A., Kawamiya, M. & Yamagata, Y. Evaluation of spatially explicit emission scenario of land-use change and biomass burning using a process-based biogeochemical model. *J. Land Use Sci*. **8**, 104–122 (2013).

[71] Mahecha, M. D., Fürst, L. M., Gobron, N. & Lange, H. Identifying multiple spatiotemporal patterns: A refined view on terrestrial photosynthetic activity. *Patt. Recogn. Let.* **31**, 2309-2317 (2010).

[72] Zscheischler, J., Mahecha, M. D., Harmeling, S. & Reichstein, M. Detection and attribution of large spatiotemporal extreme events in Earth observation data. *Ecol. Inform.* **15**, 66-73 (2013).

[73] Seneviratne, S., et al. Changes in climate extremes and their impacts on the natural physical environment. In Managing the Risks of Extreme Events and Disasters to Advance Climate

Change Adaptation. A Special Report of Working Groups I and II of the Intergovernmental Panel on Climate Change (IPCC), (Cambridge Univers. Press, Cambridge, 2012).

[74] Zscheischler, J., et al. A few extreme events dominate global interannual variability in gross primary production. *Env. Res. Let.* **9**, 035001 (2014).

[75] Mahecha, M. D., et al. Detecting impacts of extreme events with ecological in situ monitoring networks. *Biogeosci*. **14,** 4255-4277 (2017).

[76] Thornthwaite, C. W. An approach toward a rational classification of climate. *Geograph. Rev.* **38**, 55–94 (1948).

[77] Friedl, M. & Sulla-Menashe, D. MCD12C1 MODIS/Terra+Aqua Land Cover Type Yearly L3 Global 0.05Deg CMG V006 [Data set]. NASA EOSDIS Land Processes DAAC, (2015).

[78] Yin, Z., et al. Improvement of the irrigation scheme in the ORCHIDEE land surface model and impacts of irrigation on regional water budgets over China. *J. Adv. Model. Earth Syst.* **12,** e2019MS001770 (2020).

Figures on display

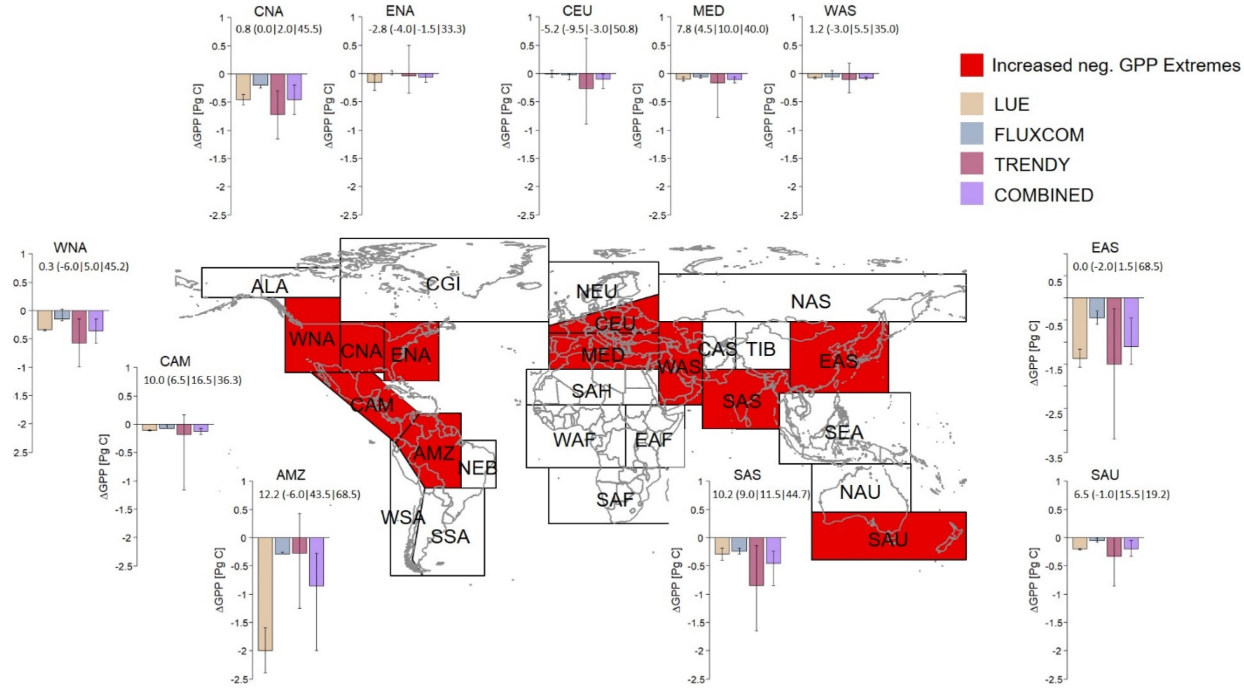

Fig. 1: Regional changes in ecosystem productivity linked to negative GPP extreme events between the 2000 – 2016 and 1982 – 1998 study periods over the IPCC regions. First, the cumulative GPP anomalies associated with negative GPP extremes were calculated for each study period separately, and then subtracted from one another (2000 – 2016 minus 1982 – 1998) to yield the changes in negative GPP extremes (ΔGPP [Pg C]). Regions that experienced a consistent increase in ΔGPP in all three data sets are highlighted (red regions). Associated increased ΔGPP (expressed as negative values) for the individual data sets (barplots) were derived from the medians over the ensemble members of the corresponding data set (combined bar represents mean of these medians). Uncertainties in ΔGPP for specific data sets were estimated from the minimum and maximum ΔGPP based on the individual ensemble members (uncertainties for the combined ΔGPP were calculated as the minimum and maximum ΔGPP based on the three GPP data sets). Numbers above the bars correspond to the change in the number of events where a positive (negative) value indicates an increased (decreased) number of events presented as mean of the three data sets (minimum | maximum | number of events in the first period).

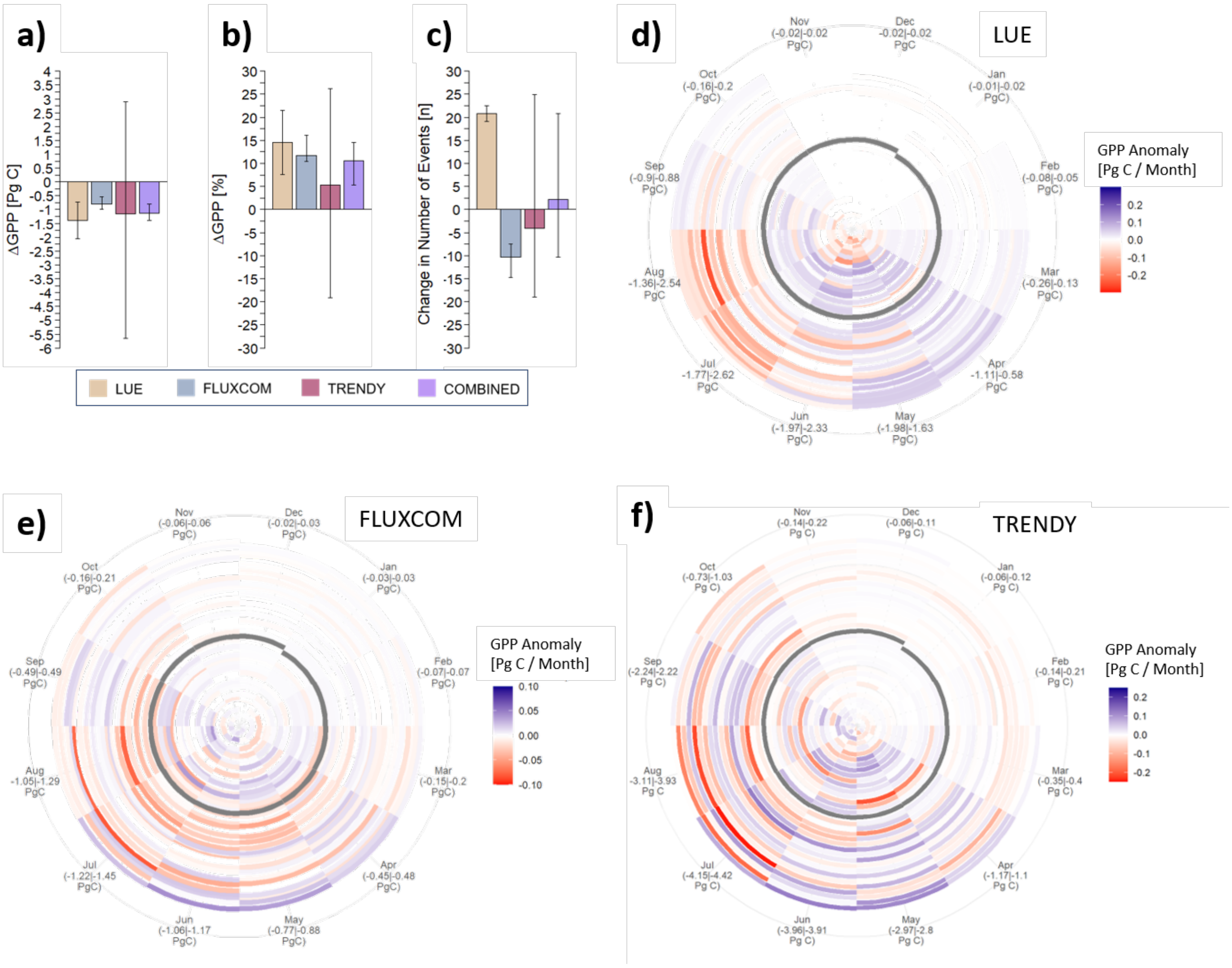

Fig. 2: **Changes in negative GPP extremes over the northern midlatitudes between the 2000 – 2016 and 1982 – 1998 study periods.** The change in negative GPP extremes was calculated as the difference in cumulative GPP anomalies linked to negative GPP extremes per study period (2000 – 2016 minus 1982 – 1998; ΔGPP). **a-b,** ΔGPP over the northern midlatitudes (23.5 – 66.0° N) expressed as **a**, Absolute [Pg C], and **b**, Relative [%] units. **c**, Changes in the number of corresponding events [n events] between the two periods. Associated ΔGPP and changes in the number of events for the individual data sets (barplots) were derived from the median over the ensemble members. The related uncertainties were estimated through the corresponding minimum and maximum (the combined information originates from the medians of the three data sets). **d-f**, Monthly anomalies in ΔGPP [Pg C /month] expressed relative to the climatological mean of the first study period for LUE (**d**), FLUXCOM (**e**) and TRENDY (**f**). The corresponding spirals start at the first entry of the time series (Jan. 1982; center) and end in December 2016 (outside) with the year 1999 masked (grey; see Methods). Outside numbers indicate cumulative monthly GPP anomalies linked to negative GPP extremes over the two study periods 2000 – 2016 (first entry) and 1982 – 1998 (second entry). Thereby, brackets denote corresponding insignificant differences between these two periods (Mann-Whitney-U test, p-value < 0.05).

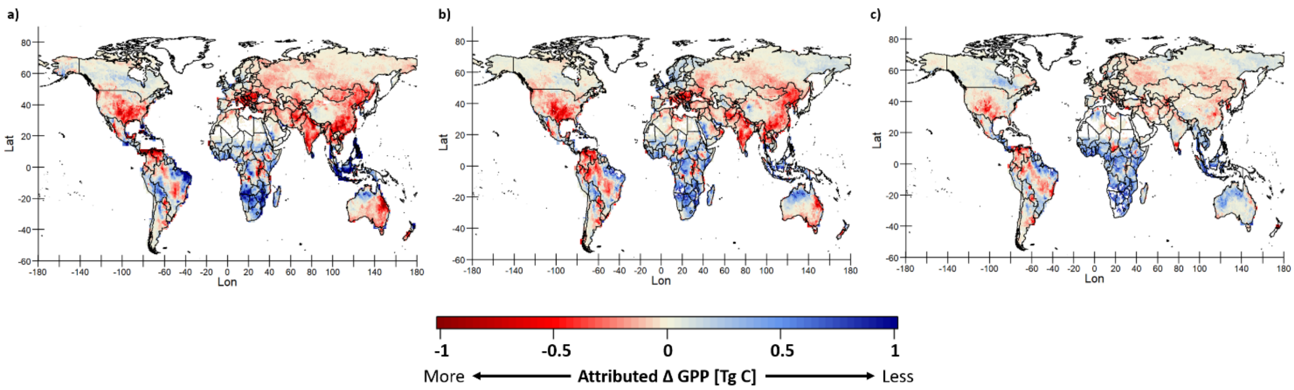

Fig.3: Changes in negative GPP extremes attributed to significant climate drivers between the 2000 – 2016 and 1982 – 1998 periods. The cumulative GPP anomalies linked with GPP extremes attributed to each of the climate drivers were calculated for each study period and then subtracted from one another (2000 – 2016 minus 1982 – 1998; attributed ΔGPP). **a-c,** The corresponding attributed ΔGPP to each of the three significant climate drivers SPEI (**a**), SPI (**b**) and concurrent low precipitation (**c**). Here, each negative GPP extreme event was attributed to all climate drivers that show significant coinciding anomalies thus the corresponding GPP anomaly potentially contributed to the balance of multiple drivers (panels). Each map was derived from the medians of the three data sets.

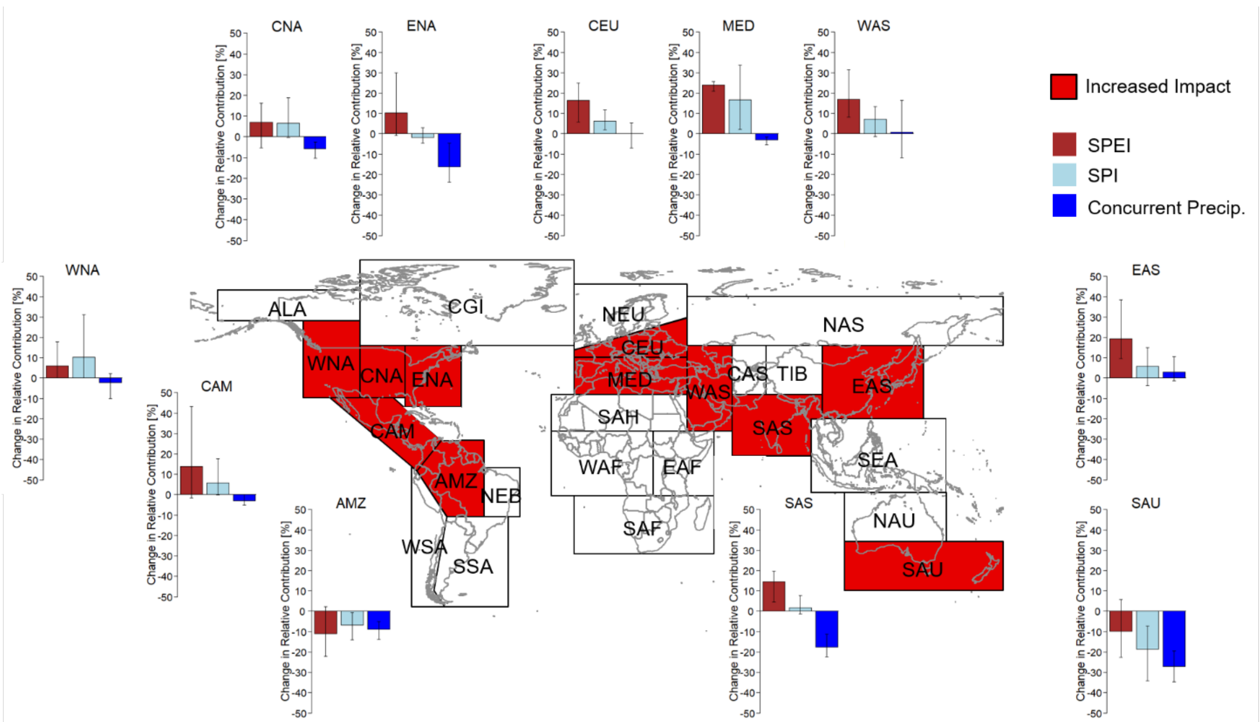

Fig. 4: Regional changes in the composition [%] of negative GPP extremes attributed to climate drivers between the 2000 – 2016 and 1982 – 1998 study periods over the IPCC regions. First, the relative contribution of GPP anomalies attributed to each of the climate drivers to the overall negative GPP extremes was calculated for each period to yield the composition of attributed negative GPP extremes. The associated changes in the composition were then expressed as the difference between the two study periods (2000 – 2016 minus 1982 – 1998). The corresponding changes between the two periods (barplots)

were derived from the median of the three data sets. Uncertainties in the composition were estimated through the corresponding minimum and maximum of the three data sets.

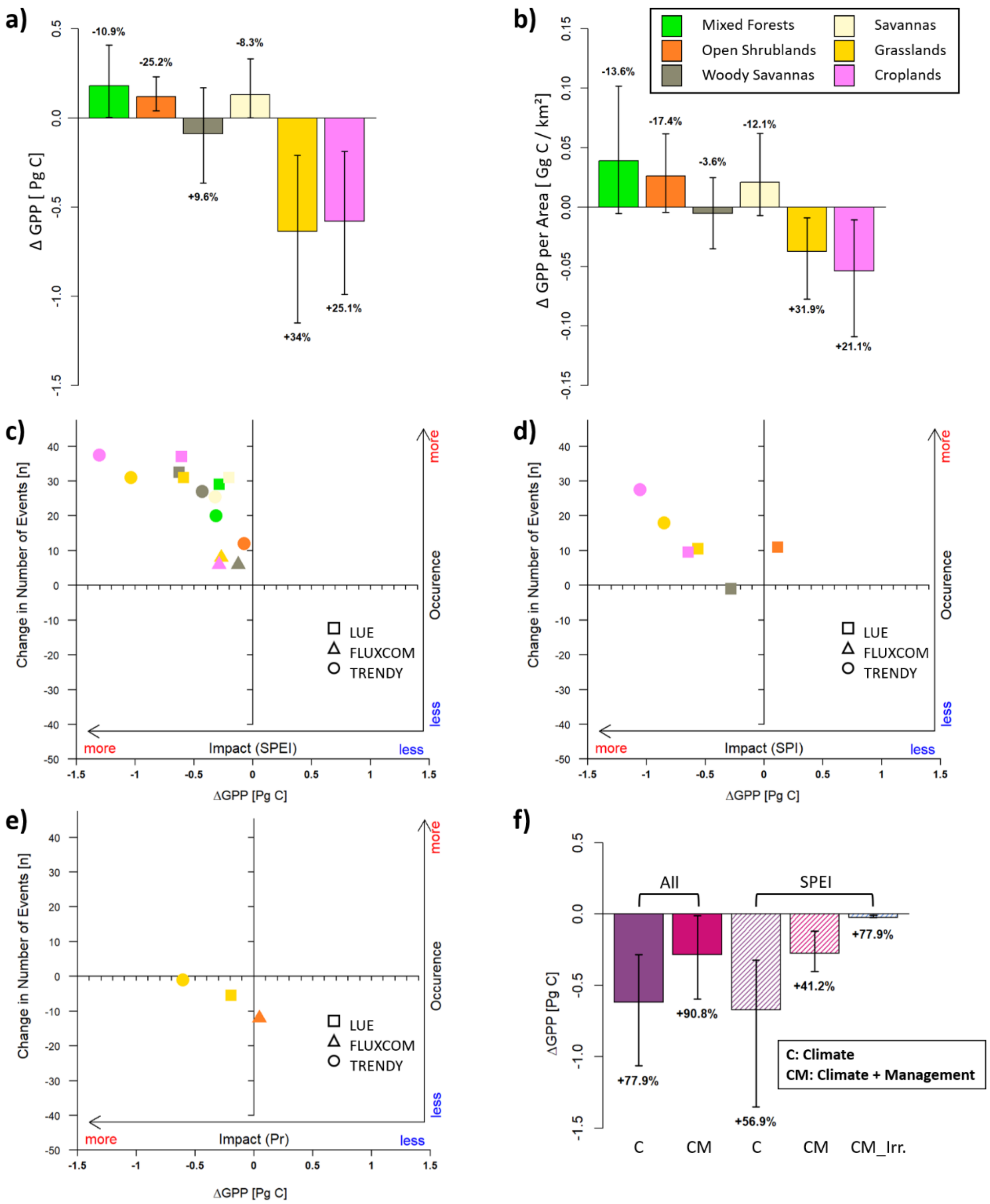

Fig. 5: Changes in negative GPP extremes for specific land covers over the northern midlatitudes between the two study periods (2000 – 2016 compared to 1982 – 1998). The change in negative GPP extremes was calculated as the difference in cumulative GPP anomalies linked to negative GPP extremes per land cover class for each study period (2000 – 2016 minus 1982 – 1998; ΔGPP). **a**, ΔGPP for distinct land covers across the northern midlatitudes (23.5 – 66.0° N) expressed as absolute units [Pg C] and **b,** normalized by the areal extent of the land cover [Gg C / km²]. Corresponding relative changes [%] (below the bars) in ΔGPP were derived from the medians of the three data sets. Uncertainties in corresponding ΔGPP were estimated as the minimum and maximum of these three medians. **c-e,** Significant (two-sided t-test, p-value < 0.05) changes in negative GPP extremes and in the number of events [n] (x-y plots) attributed to the significant climate drivers *SPEI* (**c**), *SPI* (**d**) and *concurrent low precipitation* (**e**), respectively. **f**, ΔGPP over stable cropland areas for TRENDY simulations with enabled land management options (CM)

compared to climate only simulations (C) for all climate drivers and specifically SPEI (based on three DGVMs; see Methods for details).